

Stratigraphic reconstruction and analysis of the delta remnant Kodiak in Jezero Crater, Mars

C. D. Tate¹, A. H. Hayes¹, O. A. Kanine², S. Gupta³, G. Caravaca⁴, G. Paar⁵,
S. Le Mouélic⁶, C. Traxler⁷, J.W. Rice, Jr.⁸

¹Cornell University, Department of Astronomy and Planetary Science, Ithaca, NY, USA

²California Institute of Technology Division of Geological and Planetary Sciences, Pasadena, CA, USA

³Imperial College London, Department of Earth Science and Engineering, London, UK

⁴Institut de Recherche en Astrophysique et Planétologie, CNRS, Université de Toulouse, CNES, France

⁵Joanneum Research, Institute for Digital Technology, Graz, Austria

⁶CNRS Délégation Bretagne et Pays de Loire, Nantes, France

⁷VRVis Zentrum für Virtual Reality und Visualisierung Forschungs-GmbH, Wien, Austria

⁸Arizona State University, School of Earth and Space Exploration, Tempe, AZ, USA

Key Points:

- We present a digital 3D reconstruction of Kodiak sourced from over 400 images taken by the Mars 2020 Perseverance Rover.
- This science-grade model enables precise geometric measurements of Kodiak's strata that are essential for its geological interpretation.
- Kodiak's has at least three units, of which two have bedding layers with widely varying strikes that suggest fluvial processes.

Corresponding author: Christian Tate, cdt59@cornell.edu

20 **Abstract**

21 We analyze Kodiak, an eroded delta remnant in Jezero Crater, Mars, using sev-
 22 eral hundred images from the Mastcam-Z and SuperCam instruments on the Mars 2020
 23 Perseverance Rover. We create a high-accuracy digital terrain model to measure Kodiak’s
 24 stratigraphic layers, which we divide into three units and characterize individually. While
 25 each unit possesses geometries interpreted as consistent with a Gilbert-style delta for-
 26 mation, the older units exposed on Kodiak’s north to northeast sides include more com-
 27 plex layered structures with azimuthally varying foresets. We compare Kodiak’s north-
 28 east foresets with the clinofolds of Whale Mountain, an outcrop exposed in the West-
 29 ern Jezero Delta scarp, and show similar azimuthally varying foresets. The stratigraphic
 30 analysis presented herein (strike and dip, unit thickness, etc.) will help test and refine
 31 detailed sedimentological hypotheses for the formation and evolution of the Jezero delta.
 32 Our 3D reconstruction and measurements enable unprecedented precision to evaluate
 33 depositional models and advance geological interpretation.

34 **Plain Language Summary**

35 We examine an ancient delta remnant (named Kodiak) in Mars’ Jezero Crater us-
 36 ing images from the Perseverance Rover’s Mastcam-Z and SuperCam. We created a de-
 37 tailed digital terrain model to analyze its layered structure, dividing it into several dis-
 38 tinct units. Each unit showed features typical of a Gilbert-style delta, but the older lay-
 39 ers on Kodiak’s north and northeast sides were more complex. We compared these lay-
 40 ers with similar formations. Our analysis includes detailed measurements of the layers’
 41 orientation and thickness and will refine our understanding of how the Jezero delta formed
 42 and evolved. This work required close collaboration among different teams operating the
 43 rover and its instruments. Despite camera calibration and image correlation challenges,
 44 our 3D models provide a precise view of Kodiak’s geology, offering new insights into the
 45 Martian landscape.

46 **1 Introduction**

47 Kodiak is an 80 m tall and 250 m wide butte located less than a kilometer south
 48 of the Jezero Western fan scarp (Mangold et al. (2021)). The Western Jezero Delta, ra-
 49 diating from Neretva Vallis, was once likely connected to several hills or knobs scattered
 50 within a 10 km radius of the Neretva Vallis inlet before undergoing significant erosion
 51 (Schon et al. (2012); Goudge et al. (2015)). One such remnant, Kodiak, was continuously
 52 visible to the Perseverance rover throughout the first two years of the Mars 2020 mis-
 53 sion and contains sedimentary strata that chronicle a portion of the depositional history
 54 of Jezero Crater and have been interpreted as indicators of an ancient lake environment
 55 (Mangold et al. (2021); Farley et al. (2022)). Kodiak’s exposed bedforms (Fig. 1) were
 56 fortunately perpendicular to the rover traverse for this portion of the mission and, there-
 57 fore, in a favorable alignment for rover-based imaging and long-baseline stereo reconstruc-
 58 tion. Herein, we describe our new application of structure from motion (SfM) to over
 59 400 images to generate a three-dimensional (3D) model of Kodiak’s exposed stratigra-
 60 phy. We use this Digital Terrain Model (DTM) to determine stratigraphic relationships
 61 in the Kodiak deposit and interpret the strike and dip of exposed beds in the context
 62 of a typical Gilbert-style delta.

63 Visualizing and characterizing geological features in three dimensions is crucial for
 64 their complete interpretation, and the lack of realistic and flexible rendering is a signif-
 65 icant challenge for exploring remote, human-inaccessible locations like Mars. Recently,
 66 planetary geomorphologic studies have begun using Structure-from-Motion photogram-
 67 metry (SfM) to create 3D Digital Terrain Models (DTMs) of Martian terrains, such as
 68 the Kimberley outcrop (Caravaca et al. (2020)) and the Glen Torridon region (Caravaca

69 et al. (2022)) in Gale Crater, that can be visualized in virtual reality (VR) environments
70 for a more immersive and realistic experience of the terrain with its spatial relationships
71 (e.g., Caravaca et al. (2020)). More traditionally, stereo photogrammetric processes are
72 used to create DTMs on which researchers perform geometric analysis (e.g., Barnes et
73 al. (2018); Banham et al. (2018, 2022); Traxler et al. (2022); Paar et al. (2023)) using
74 software such as P_{Ro}3D (Traxler et al. (2022)) to obtain geometric measurements in-
75 cluding strike and dip for each layer. While VR-compatible DTMs offer a rich visual con-
76 text for qualitative geological interpretation (Barnes et al. (2018)), they cannot reach
77 their full scientific potential without permitting quantitative analysis of layer thickness,
78 dip angles, strike azimuths, and other geometric properties. Herein, we discuss a pro-
79 cess that combines the immersive experience of the VR-compatible DTMs with the quan-
80 titative analysis of traditional DTMs to analyze Kodiak.

81 Early in its mission, the Mars 2020 Perseverance Rover documented Kodiak's East
82 and North faces from various perspectives (Figs. 1 and 2). We use the data collected dur-
83 ing this campaign to create a high-resolution DTM optimized for immersive VR en-
84 vironments and stratigraphic analysis tools such as P_{Ro}3D. We then use the model to
85 measure the dimensions and orientations of various bedding packages observed in Ko-
86 diak's exposed stratigraphy. We build on the methodologies of prior studies (Caravaca
87 et al. (2020); Barnes et al. (2018); Banham et al. (2018)) by combining the improved ac-
88 curacy of multi-view SfM photogrammetry with a complete 3D analysis workflow to con-
89 strain Kodiak's stratigraphic relationships and interpret the strike and dip of exposed
90 bedding layers in the context of a typical Gilbert-style delta. The DTMs, rendered or-
91 thographic mosaics, and plane measurements provided herein are used in other studies
92 (Caravaca et al. and Kanine et al., both in this issue). These papers go beyond our present
93 research and evaluate specific sedimentologic scenarios to explain our observations and
94 measurements.

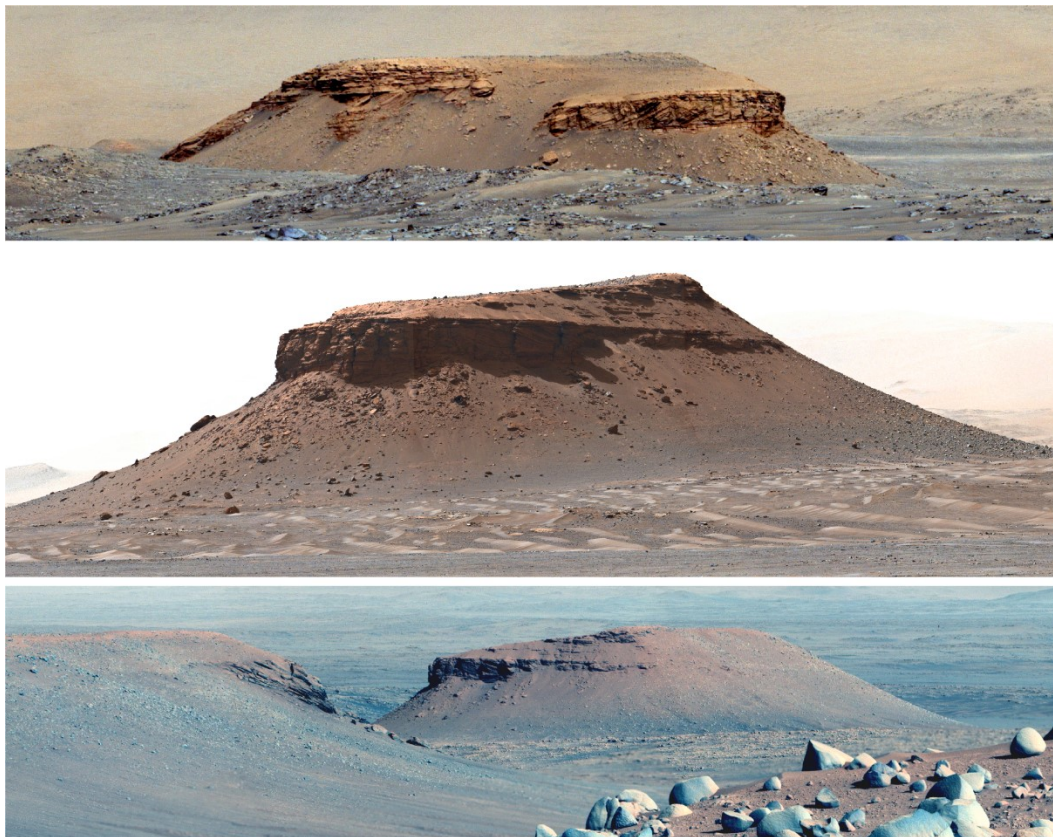


Figure 1. Mastcam-Z mosaics of Kodiak from several perspectives: (a) showing the eastern outcrops on Sol 83 (earth date), (b) northern outcrops on Sol 409 (April 14, 2022), and (c) the northwest side from Sol 753 (April 3, 2023) after climbing the delta and gaining 130 m of elevation. The structure on the left of (c) is the southern side of Whale Mountain. Image credits: NASA/JPL/MSSS/ASU.

2 Data

Our process uses radiance-calibrated (RAD) images taken from Sol 4 to Sol 580 (March 1, 2021 to Oct. 7, 2022) with two science instruments on the Mars 2020 Perseverance rover: the Mastcam-Z multispectral stereo imagers (Bell et al. (2021); Hayes et al. (2021); Kinch et al. (2020)) and SuperCam’s Remote Micro-Imager (RMI) Maurice et al. (2021). The SuperCam RMI has a field of view (FOV) of about 1° with a pixel instantaneous field of view (IFOV) of $10\mu\text{rad}$ (Maurice et al. (2021); Wiens et al. (2021)). Although RMI images have more resolving power than the Mastcam-Z’s, even at their highest zoom of 110 mm focal length (6° FOV and $67\mu\text{rad}$ IFOV, Hayes et al. (2021)), this comes at the expense of a restricted FOV. The best Mastcam-Z resolution on Kodiak is from a distance of 480 m, where its horizontal pixel scale is 3.3 cm. Kodiak’s eastern outcrops were imaged from farther distances (1.9-3.2 km), with a best pixel scale of 13 cm.

This Kodiak imaging campaign required coordination between SuperCam, Mastcam-Z, and rover operations teams. As Perseverance progressed along its route and new perspectives of Kodiak came into view, the Mars 2020 science team requested observations to fill gaps in the butte’s coverage. The imaging resolution of Kodiak varies across the campaign according to Perseverance’s traverse; Table 1 summarizes Kodiak’s Mastcam-

113 Z dataset and gives the estimated values for the resolution of each region of Kodiak cap-
 114 tured. The reconstructed model shown in Fig. 3 uses over 400 Mastcam-Z images of Ko-
 115 diak and its surrounding terrain along the rover traverse (shown in Fig. 2). Additional
 116 structural and textural detail comes from 52 SuperCam RMI images captured from six
 117 unique locations (Table S2).

118 The first 400 sols of the Mars 2020 mission included the Crater Floor Campaign
 119 (Horgan et al. (2023)), during which Perseverance imaged Kodiak’s eastern face from
 120 azimuths between 65° to 102° and distances between 1.8 km and 2.6 km. Images from
 121 the Delta Front and Sample Depot campaigns Prepared by the Mars Sample Return Cam-
 122 paign Science Group (MCSG) et al. (2023) on sols 400-715 saw Kodiak’s northern face
 123 from -36°N to 19°N azimuth and between 0.5 and 1.1 km distance and from an average
 124 of 32 m higher elevation than previous campaigns. The relative illumination and view-
 125 ing geometries of Kodiak and the rover determined the most scientifically valuable time
 126 of day to take the images. The best images of eastern Kodiak in the first 400 sols were
 127 taken in morning lighting, while the best images of the often highly shadowed northern
 128 outcrops had evening illumination. We do not use images taken after Sol 700 because
 129 they have lower spatial resolution and do not significantly expand the coverage of Ko-
 130 diak’s most exposed outcrops.

131 Three dual-instrument sequences taken on Sols 63, 248, and 580 form the core of
 132 this dataset. Together, these images document about two-thirds of Kodiak. This region
 133 includes most of Kodiak’s exposed outcrops above its wide scree and talus skirt judg-
 134 ing from orbital views (Fig. 2).

135 3 Terrain Reconstruction

136 We use structure from motion (SfM) with the Mastcam-Z and SuperCam images
 137 (listed in supplementary Tables S1 and S2) to reconstruct the high-resolution digital ter-
 138 rain model (DTM) shown in Fig. 3. This model is viable and downloadable from Sketch-
 139 fab from the following link: <https://skfb.ly/oCyI8>. We pre-processed each PDS image
 140 data product with a Python script that opened, transformed, and saved the images and
 141 camera model information in formats compatible with Agisoft Metashape. The local-
 142 ized exterior camera models are the primary metadata we extract from the PDS head-
 143 ers. These encode the image’s position and orientation in a coordinate system compat-
 144 ible with the SfM software. This code used to perform this analysis is available on GitHub:
 145 <https://github.com/cdt59/MPPP>.

146 3.1 Long-baseline Stereo and Structure from Motion (SfM)

147 Long-baseline stereo techniques have precedence on Mars rover missions for cap-
 148 turing high-resolution topographic data (Caravaca et al. (2021)). These techniques typ-
 149 ically involve capturing stereo pairs of images from two distinct but well-characterized
 150 positions, often separated by large distances relative to the target, to reconstruct the 3D
 151 geometry of the terrain. Such methods have been beneficial for navigational and scien-
 152 tific documentation, as they provide a quick way to obtain depth information from a scene
 153 (Maki et al. (2020); Bell et al. (2021)). However, traditional long-baseline stereo tech-
 154 niques often rely on single-pair stereo matching, which can be susceptible to calibration,
 155 alignment, and localization errors (Hayes et al. (2011); Barnes et al. (2018)).

156 In contrast, our approach employs Structure from Motion (SfM) as implemented
 157 in Agisoft Metashape Professional, which offers several advantages (Agisoft (2019); Le Mouélic
 158 et al. (2020); Over et al. (2021); Caravaca et al. (2021); Bistacchi et al. (2022); Paar et
 159 al. (2023)) as well as industrial applications (Paar et al. (2022)). SfM uses multiple im-
 160 ages from different viewpoints to create a more self-consistent Digital Terrain Model (DTM).
 161 This method minimizes errors globally across the dataset by comparing tie points in one

162 image to every other overlapping images, solving for each image’s highest confidence depth
 163 map (Agisoft (2019); Over et al. (2021); Caravaca et al. (2021)). The resulting 3D model
 164 is more accurate and comprehensive because it minimizes camera model errors over all
 165 images and control points. Thus, while long-baseline stereo provides a robust but some-
 166 times limited snapshot of the Martian terrain, our SfM approach creates a more detailed
 167 and accurate 3D reconstruction.

168 3.2 Rover Localization

169 Perseverance operations align each end-of-drive location with a Mars 2020 basemap
 170 and make these rover waypoints available for science analysis. The Mars 2020 basemap
 171 is made from a mosaic of orbital HiRISE images and has a resolution of about 25 cm (Stack
 172 et al. (2020); Farley et al. (2020)). Accurate rover and camera localization are required
 173 to generate precise models at their location, orientation, and scale. The estimated po-
 174 sition and orientation of the image are made in Site Frame as obtained from the JPL lo-
 175 calization process (Calef et al. (2023); Crumpler et al. (2023); Ruoff, N. A., Deen, R. G.,
 176 Pariser, O. (2023)) to ensure that the SfM algorithm has the best available initial cam-
 177 era models for correctly triangulating points in space, thereby generating a reliable and
 178 high-fidelity 3D model. Inaccurate localization data can introduce errors in the recon-
 179 structed geometry, leading to distortions or misalignments in the resulting DTM. More-
 180 over, precise localization allows for effectively merging data from different imaging cam-
 181 paigns or instruments, such as Mastcam-Z and SuperCam’s Remote Micro-Imager, into
 182 a single, coherent model. This is particularly crucial when the model aims to capture
 183 complex geological features like the strata exposed at Kodiak.

184 3.3 Reconstruction Error

185 Two sources of error dominate the accuracy and precision of 3D reconstructions:
 186 uncertainties in the geometric camera model and range errors originating from correla-
 187 tion uncertainties. Although the Mars 2020 cameras are robustly calibrated in the rover
 188 coordinate system (Maki et al. (2020); Hayes et al. (2021)), the absolute camera posi-
 189 tions are less constrained in the Mars-fixed coordinate system in which the vehicle es-
 190 timates its position and orientation as it drives through the terrain. This introduces pro-
 191 jection errors that structure from motion mitigates by optimizing camera parameters in
 192 a global control network. These projective errors are distinct from a second source: range
 193 error, the precision with which a stereo pair of images can correlate features and esti-
 194 mate their position in space with triangulation. Range error is in the line-of-site or range
 195 direction and increases quadratically for a fixed stereo base length. Because range er-
 196 ror only quantifies the sub-pixel correlation between two stereo images, it is not a valid
 197 estimate of a model’s overall reconstruction quality. Nevertheless, we assume that range
 198 errors are the primary source of non-correlated errors. As such, range error limits the
 199 relative position of points on the model surface for plane-fitting strike and dip analysis.

200 The theoretical range error is a standard but limited measure of reconstruction er-
 201 ror. Similar to how imaging resolution estimates the precision of the image projection
 202 onto the model, the range error estimates the precision in the third axis (i.e., the range
 203 axis, which is orthogonal to the image’s line and sample axes). Each well-characterized
 204 stereo pair can yield a digital terrain model (DTM) with a pixel-by-pixel accuracy de-
 205 termined by the camera properties and the relative geometry of imaging locations and
 206 the terrain. We estimate range errors for this model are comparable to the pixel scale,
 207 which is 3.3 and 13 cm for Kodiak’s north and east faces, respectively (Table 1). Fur-
 208 ther details about our methodology for estimating the 3D reconstruction error are in S2
 209 of the online supplementary materials.

Table 1. Summary of the Mastcam-Z observations of Kodiak, which we separate into four azimuth ranges relative to Kodiak. These are limited to Mastcam-Z sequences taken at its highest resolution zoom level at 110mm.

	East	Northeast	North	Northwest
sol range	004 – 275	382 – 388	409 – 711	750 – 756
imaging locations ¹ , total	23	3	11	3
imaging locations ¹ , used ²	8	3	6	0
SuperCam locations ³ , total	3	0	3	0
preferred time of day ⁴	morning	morning	afternoon	evening
local mean solar time	7:58 – 11:38	8:10 – 9:36	10:04 – 16:00	11:46 – 16:03
local mean solar time, average	10:20	9:10	13:20	14:30
range ⁵ [km]	1.8 – 2.4	2.5 – 3.2	0.48 – 1.1	2.4 – 2.5
range ⁵ , average [km]	2.2	2.8	0.71	2.5
elevation [m]	-5.3 – 1.8	-1.3 – 2.2	21 – 48	127 – 133
elevation, average [m]	0.0	0.3	32	130
azimuth ⁶ [°North]	84° – 102°	64° – 79°	324° – +19°	315° – 320°
azimuth ⁶ , average [°North]	92°	73°	348°	318°
pixel scale, average [cm/pixel]	15	19	4.8	17
pixel scale, best [cm/pixel]	12	17	3.2	16
range error ⁷ , average [cm]	140	98	4.4	160
range error ⁷ , best [cm]	35	24	2.2	55

¹ See Table S1 or the online spreadsheet for details on each Mastcam-Z sequence.

² The values below are only for used sequences. See Table S1.

³ This is the total number of SuperCam RMI sequences taken in each region. See Table S2 for details. All other information in this table is for the Mastcam-Z sequences.

⁴ The Sun’s incidence angle is important for capturing the fine details on Kodiak because of its many vertical outcrops. The preferred time of day is when the outcrop is best illuminated, which happens when the Sun is approximately behind the camera.

⁵ We calculate range as the distance from the rover’s location to a reference point in Kodiak (the center of curvature of Unit 1, which we assume to be 2335 m West, 244 m South, and 50 m above the O.E.B. landing site). See the downloadable supplementary spreadsheet for each imaging location’s relative Northing, Easting, and Elevation.

⁶ We calculate azimuth as the clockwise angle from North to a reference point in Kodiak (the center of curvature of Unit 1).

⁷ See section S2 for how we calculate range error and recommend interpreting it.

210

3.4 Geometric measurements

211

212

213

214

215

216

217

218

219

220

We inspect and annotate the model using the Planetary Robotics 3D Viewer software abbreviated P_{RO}3D (Barnes et al. (2018); Traxler et al. (2022)). The P_{RO}3D software imports DTMs and provides several annotation tools that we use to trace the outcrop layers and measure their strike and dip angles. P_{RO}3D uses the plane-fitting algorithm to calculate layer orientation and error. This algorithm uses principal component analysis (PCA) described in (Quinn & Ehlmann (2019)) to constrain layer geometry and estimate measurement uncertainty. Additional information about P_{RO}3D and annotation files used for our measurements can be found in S3 and S4. The XYZ points extracted from our layer tracings are available in the supplementary materials for future researchers who want to use alternative methods for determining layer orientation.

221

4 Results

222

223

224

225

226

We divide the stratigraphy of Kodiak butte into three units, each containing inclined beds bounded by sub-horizontal beds and separated by truncation surfaces. We adopt the naming convention used in Caravaca et al. (this issue) and describe Units 0, 1, and 2 in stratigraphic order, as shown in Fig. 3. Table 2 lists each unit’s average sequence thickness, dip, and strike measurements.



Figure 2. The Mars 2020 basemap of the Jezero Crater (primarily made from HiRISE mosaics) and the traverse of the Perseverance rover for the first 715 Sols of the Mars 2020 mission. The white dots show the locations where the rover stopped to take images, and the blue and black symbols show the positions and pointing of the Mastcam-Z images used to reconstruct Kodiak.

227

4.1 Unit 0

228

229

230

231

232

233

234

235

236

237

Unit 0 outcrops on the northwest flank of Kodiak butte. Scree covers its lower layers, making it the only unit without visible bottomsets. Unit 0 consists dominantly of variably inclined strata that extend laterally for about 60 m, as measured from our SfM model. It shows average and maximum thicknesses of 2.5 and 3.7 m, respectively. A convex-up sedimentary body in the center of Unit 0 is 6 m wide and 1 m high and has inclined layers on both flanks. Overlying this convex-up feature, we measure a range of dips between 15 to 25°, predominantly towards the northeast, at 35°N. At the east side of the outcrop, Unit 0's foresets are truncated by onlapping inclined layers of Unit 1. On top of the inclined layers, a sub-horizontal erosion surface separates them from sub-horizontal topset beds. These topsets appear to be stratigraphically equivalent to Unit 1's topset.

238

4.2 Unit 1

239

240

241

242

243

Unit 1 outcrops Kodiak's northeast flank. The lower part consists of over 5 m of sub-horizontal strata that dip $\sim 5^\circ$ approximately to the south $\sim 179^\circ$ N. Another apparent outcrop of Unit 1's sub-horizontal strata occurs lower on the northeast corner of the butte. These layers appear to be in place, indicating about 10 m of sub-horizontally stratified rocks within the lower part of Unit 1.

244

245

246

247

248

249

250

251

252

253

254

The inclined beds of Unit 1 extend over 160 m from the middle of Kodiak's northern face to the middle of its eastern face. These layers have a range of dip azimuths between 180°N and $\sim 250^\circ$ N at Unit 1's southern and western extents, respectively. The inclined layers on the northwest side of Unit 1 onlap the inclined layers of Unit 0. At this interface between Units 1 and 0, the bedding dip azimuths are approximately opposite. Cobble-sized clasts (0.1-0.2 m in diameter) are embedded in Unit 1 close to this boundary, and these rounded grey clasts stand out against the nominal red appearance of Kodiak's strata. The inclined strata in the rest of Unit 1's northern exposure show a 6-7.2 m thick section of sigmoidal layers. Although the dip and strike geometries are complex to constrain on this flat outcrop face, they are consistent with dip azimuths to the southwest (Fig. 3).

255

256

257

258

259

260

261

262

263

264

Kodiak's strata at its northeast corner (or "nose") appear to be plunging into the outcrop. This is the boundary between Unit 1 north and east inclined layers, which we characterize as the point of greatest dip azimuth divergence. The outcrop at this crucial location is weathered, crumbly, and only obliquely imaged in shadow. Despite these difficulties, our reconstructed model reveals a doming pattern that is not apparent from the separate inspection of the original images. The inclined beds dip in divergent directions on both sides of this junction. Unit 1 North dips towards $\sim 230^\circ$ N, and Unit 1 East dips towards 180°N. The latter contains the tallest and steepest inclined beds measured on Kodiak, at about 9 m tall and 40° dip towards the south. At the southern extent of Unit 1, the inclined beds shallow to dip angles of about 10°.

265

266

267

268

The upper sub-horizontal layers appear equivalent across both sides of Unit 1's east-north junction and with the topsets of Unit 0. However, on the southern end of Unit 1, the truncation surface appears to fade as the overlying strata drapes more continuously with the shallowly dipping inclined beds below.

269

4.3 Unit 2

270

271

272

273

274

Unit 2's lower sub-horizontal layers appear continuous with Unit 1's inclined beds, although scree covers large areas separating these two units. This package is up to 10 m thick, making it the thickest sub-horizontal part of Kodiak. This outcrops in the middle of Unit 2 and at its southern extent. The inclined beds of Unit 2 range between 2 to 5.6 m thick with an average of 4 m. Like Unit 1, the southernmost beds are shallow

275 to about 10° dip. Unlike Unit 1, however, all the inclined strata dip towards a consis-
 276 tent azimuth of 135°N .

277 The sub-horizontal layers overlying Unit 1 are inclined at an average dip of 4.1°
 278 towards the same azimuth of 134°N . At the interface of the inclined strata and overly-
 279 ing sub-horizontal strata, scouring and crossbedding are observed. Unit 2 also outcrops
 280 on Kodiak's north side above Units 0 and 1. Here, the strata show cross-bedding simi-
 281 lar to the equivalent layers on Kodiak's southern end. However, the orientation of these
 282 exposures to their probable dip directions is not favorable for reliable measurements of
 283 dip and strike.

284 4.4 Unit 3

285 Unit 3 is a deposit of boulders and cobbles overlying Unit 2's topsets. The most
 286 visible boulders have 0.5 m diameters, and we measure the largest as wide as 2 m. There
 287 does not appear to be any strata in Unit 3; hence, we do not include it in Table 2.

Table 2. Measurements on the 3D reconstruction of Kodiak. These give the horizontal scale of each major sequence, the number of strike and dip measurements on suitable outcrops, and their average values of dip angle and azimuth. After projecting each vector into the horizontal plane, we calculated the average azimuth values. Kodiak is divided into three units, as illustrated in Fig. 3, with Unit 1 further differentiated between east and north to highlight its variation in dip azimuth directions.

	Unit 0	Unit 1, North	Unit 1, East	Unit 2
Mastcam-Z resolution [cm]	3.3	3.3	18	13
outcrop exposure width [m]	60	80	100	120
topset height [m]	2.0	2.0	2.5	9.7
topset measurements	3	9	5	48
topset dip [$^\circ$]	5.7	4.9	5.4	4.1
topset azimuth [$^\circ\text{N}$]	342	347	232	134
foreset height [m]	2.5	5.9	7.7	4.0
foreset max height [m]	3.7	7.2	9.0	5.6
foreset measurements	11	29	40	21
foreset dip [$^\circ$]	18.8	29.2	28.1	27.0
foreset azimuth [$^\circ\text{N}$]	35	229	180	135
bottomset height [m]	-	>3	>2	10
bottomset measurements	-	1	9	3
bottomset dip [$^\circ$]	-	~ 8	4.5	~ 6.6
bottomset azimuth [$^\circ\text{N}$]	-	~ 160	179	~ 148

288 5 Discussion

289 Our 3D digital outcrop model of Kodiak butte provides an unprecedented oppor-
 290 tunity to measure the quantitative geometry of its exposed layers. In Unit 2, Kodiak shows
 291 structures consistent with the previously proposed Gilbert delta model (Mangold et al.
 292 (2021)), with the central section comprising foreset beds that smoothly transition into
 293 bottomset strata at their base and overlying topset strata that abruptly terminate the
 294 foresets at their top. The foreset beds in Unit 2 show a consistent dip of 30° to the south-
 295 east, while the topsets and bottomsets dip about $3\text{-}8^\circ$ in the same direction. These ob-
 296 servations alone suggest a Gilbert-style delta depositional model for Kodiak with the delta
 297 lobe prograding basinward from the Neretva Valis inlet to the southeast at 140°N .

298 Within Units 0 and 1, however, the layers appear to have a more complex struc-
 299 ture than the typical Gilbert-style deltaic succession shown in Unit 2. Not only does Unit
 300 1's bedding azimuths change throughout the exposure, but these dip angles are also the

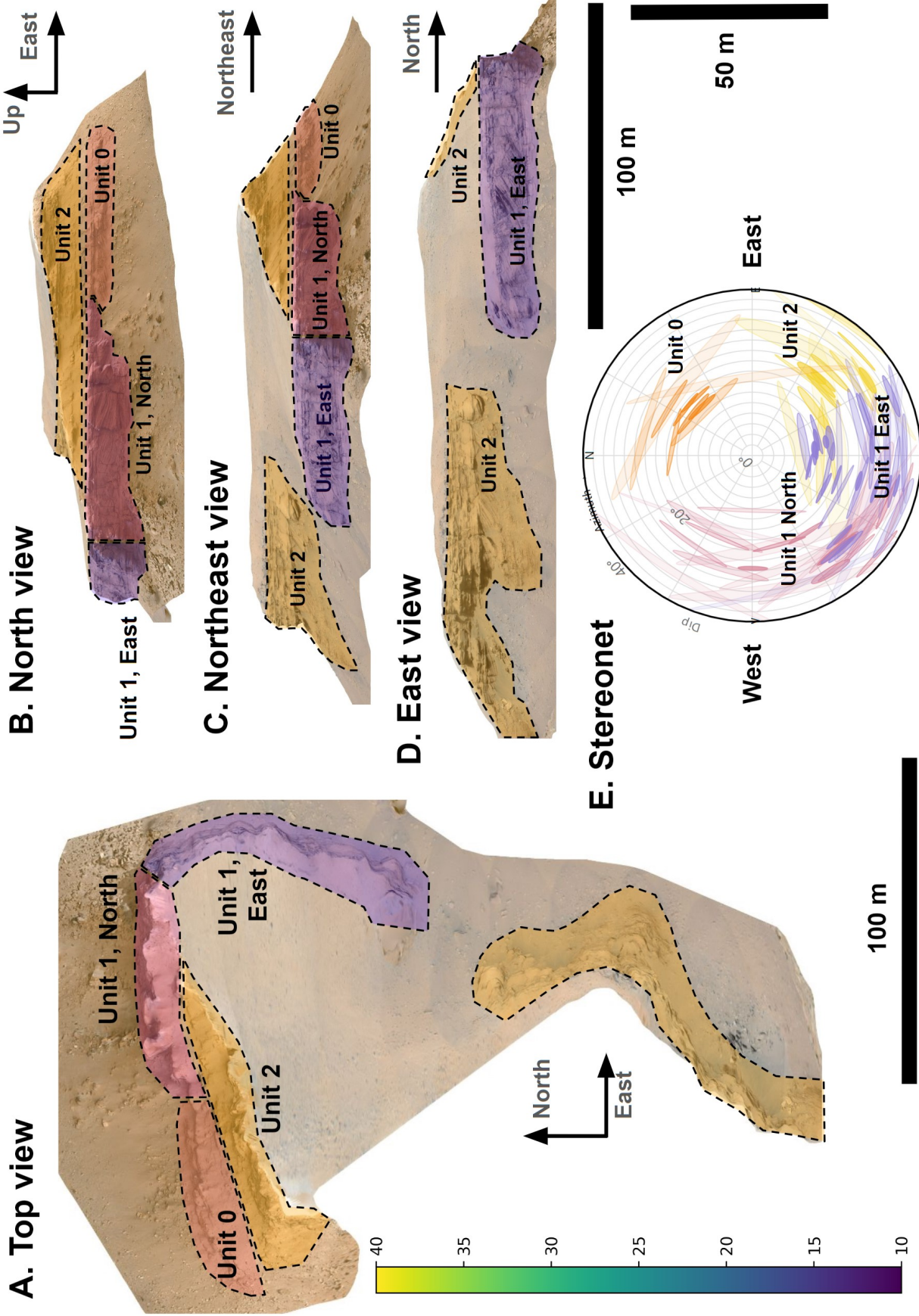


Figure 3. Rendered images of Kodiak's 3D reconstruction. Dashed lines show the approximate boundaries of Kodiak's three stratigraphic units. (a) is a vertical orthographic projection of Kodiak with superimposed strike and dip symbols showing the dip magnitudes and azimuth orientations for each unit characterized in this study. The side views of Kodiak are orthographic projections (b) from the north, azimuth $0^\circ N$, (c) from azimuth $45^\circ N$, and from the east, azimuth $90^\circ N$. (e) Stereonet of the foreset strike and dip measurements with their error ellipses Quinn & Ehlmann (2019).

301 steepest measured at Kodiak. Foreset strata in Units 0 and 1 indicate different accre-
 302 tion directions across a small lateral extent (~ 50 meters), indicating deposition within
 303 narrow, overlapping delta lobes (Caravaca et al., this issue). The foresets of unit 1 also
 304 have the greatest thickness on Kodiak, with a 9.0 m maximum foreset thickness on its
 305 eastern face. As seen in Table 2, these vertical heights are considerably larger than Units
 306 0 and 2. These measurements on Units 0 and 1 reveal geometrical complexity that may
 307 challenge a deltaic depositional hypothesis for Kodiak (see Kanine et al., this issue).

308 **5.1 The narrow deltaic lobe interpretation**

309 Unit 1 contains foreset beds that diverge $\sim 60^\circ$ in azimuth over a horizontal dis-
 310 tance of less than 50 m. This suggests that the original geometric planform of the foreset-
 311 containing sedimentary body was a relatively narrow lobate, convex-up form. Meanwhile,
 312 Unit 0 has irregular structures and an average dip direction of foreset beds opposite to
 313 Unit 1, indicating that it represents a different sedimentary body that accreted in an other
 314 direction. The northeast "nose" of Kodiak's Unit 1 could be a delta lobe that prograded
 315 to the southwest. Although its ~ 50 m radius of curvature is narrow for a delta lobe, this
 316 scale is consistent with a relatively young lobe (Barrett et al. (2020)).

317 **5.2 Comparisions to the main Western delta front**

318 The leading Western delta front contains foreset structures similar to those observed
 319 at Kodiak. Whale Mountain (SF model), for instance, is the closest part of the West-
 320 ern Delta to Kodiak. Fig. S4 shows Whale Mountain's dip directions and how their ra-
 321 dius of curvature has a similar ~ 50 m scale as the diverging clinoforms we measured on
 322 the northeast side of Kodiak's Unit 1. While Kodiak's outcrop is neither well-preserved
 323 (highly weathered and degraded) nor well-imaged (in shadow and foreshortened by its
 324 off-normal orientation relative to the imaging direction), Whale Mountain presents a clean,
 325 vivid outcrop. Mastcam-Z imaged it on Sol 614 in optimal illumination and 1 cm/pixel
 326 (more than three times finer resolution than the best on Kodiak). Images from the delta
 327 top campaign imaged the western side of Whale Mountain (Sols 753, 756, 762), and show
 328 that its dip azimuths diverge a total of $\sim 180^\circ$. This is a more extreme dip azimuths di-
 329 vergence than the $\sim 50^\circ$ measured on Kodiak. If there is a valid comparison between the
 330 narrow delta lobe interpretation of Kodiak Unit 1 and the similar structure of Whale Moun-
 331 tain, then studying the latter could be essential to understanding Kodiak.

332 Other structures on the delta front have foresets with vertical outcrops of over 20
 333 m, which are far taller than Kodiak's maximum foreset height of 10 m. These locations
 334 on the delta front (in order of closest to farthest from Kodiak) are Mount Juhle (imaged
 335 on Sol 614, 625) (<https://skfb.ly/ozZ9P>), Franklin Cliff (Sol 696, 704) <https://skfb.ly/oMpYF>),
 336 and finally the Minors Castle and Morro Rock area (Sol 397, 398) on the easternmost
 337 extent of the Western Delta <https://skfb.ly/oJp8U>). Franklin Cliff is especially interest-
 338 ing for its preserved contact between foresets and topsets. These and other structures
 339 on Jezero's Western delta front are analyzed by Gupta et al. (this issue). Future stud-
 340 ies should examine the deltaic environment required to produce horizontally curving fore-
 341 sets and how deltaic advancement could be toward the southwest, and compare these
 342 findings with evidence in the Western delta.

343 **5.3 Comparisions to other delta rements**

344 Two other remnants named Dragonera and Cabrerae stand southeast of Kodiak.
 345 Although smaller and more weathered than Kodiak, Cabrerae contains outcrops south-
 346 west dipping foresets and bottomsets similar to those seen on Kodiak (albeit ~ 50 me-
 347 ters lower elevation). Dragonera and the more distal remnants, such as Santa Cruz (im-
 348 ages on Sols 36, 123) and Isle Royale (Sol 676) to the east and Pilot Pinnacle (Sol 128)
 349 to the south, are smoother and do not have analogous outcrops. It is unknown what causes

350 this range of geomorphic expressions (Goudge et al. (2018); Quantin-Nataf et al. (2023)),
 351 but we find inclined beds resembling foresets only on the two remnants closest to the West-
 352 ern Delta.

353 6 Conclusion

354 We present a detailed 3D digital outcrop model of the Kodiak butte created from
 355 the fusion of hundreds of Perseverance Rover images. Stratigraphic analysis of the re-
 356 sulting DTM expands upon previous interpretations of Kodiak as deposits from a Gilbert-
 357 style delta with quantitative measurements. Our study shows the foreset strike azimuths
 358 change systematically over Kodiak’s north and northeast outcrops. The depositional en-
 359 vironments preserved in Kodiak are related to the enormous Western Delta fan, and in-
 360 vestigating Kodiak can advance our understanding of Jezero’s other deltaic structures
 361 throughout the crater floor.

362 7 Data Availability Statement

363 This study utilizes data from Mars rover imaging, which are archived and acces-
 364 sible through the Planetary Data System (PDS). The end data products derived from
 365 these images and our processing are included in the supplementary materials of this ar-
 366 ticle for ease of reference and use. In adherence to the FAIR Data principles, we ensure
 367 that our data is Findable, Accessible, Interoperable, and Reusable. Descriptions and ac-
 368 cess instructions for all other utilized data and software tools, which are publicly avail-
 369 able, and can be found in (Tate, 2023).

370 Acknowledgments

371 The Mars 2020 Mastcam-Z and SuperCam teams were tremendously influential in
 372 collecting and formatting these images. Another thanks to NASA’s Planetary Data Sys-
 373 tem (PDS), from which all the data used in this study are publicly available. The JPL
 374 Mars 2020 Localization Team provided the localization and pose for each Perseverance
 375 rover end-of-drive location. Joanneum Research and VRVis receive funding from the Aus-
 376 trian Research Promotion Agency, ASAP-18 Project 892662 “Mars-3D”. VRVis is funded
 377 by BMK, BMAW, Styria, SFG, Tyrol, and Vienna Business Agency in the scope of COMET
 378 - Competence Centers for Excellent Technologies (879730), which FFG manages.

379 References

- 380 Agisoft, L. L. C. (2019). Agisoft metashape user manual: Professional edition. *Ver-*
 381 *sion*.
- 382 Banham, S. G., Gupta, S., Rubin, D. M., & others. (2022). Evidence for fluctuat-
 383 ing wind in shaping an ancient martian dune field: The stimson formation at the
 384 greenheugh pediment, gale crater. *Journal of*.
- 385 Banham, S. G., Gupta, S., Rubin, D. M., Watkins, J. A., Sumner, D. Y., Edgett,
 386 K. S., ... Vasavada, A. R. (2018, June). Ancient martian aeolian processes and
 387 palaeomorphology reconstructed from the stimson formation on the lower slope of
 388 aeolis mons, gale crater, mars. *Sedimentology*, 65(4), 993–1042.
- 389 Barnes, R., Gupta, S., Traxler, C., Ortner, T., Bauer, A., Hesina, G., ... Tao, Y.
 390 (2018, July). Geological analysis of martian rover-derived digital outcrop models
 391 using the 3-D visualization tool, planetary robotics 3-D viewer-PRo3D. *Earth*
 392 *Space Sci.*, 5(7), 285–307.
- 393 Barrett, B. J., Gawthorpe, R. L., Collier, R. E. L., Hodgson, D. M., & Cullen, T. M.
 394 (2020, February). Syn-rift delta interfan successions: Archives of sedimentation
 395 and basin evolution. *Depositional Rec.*, 6(1), 117–143.

- 396 Bell, J. F., 3rd, Maki, J. N., Mehall, G. L., Ravine, M. A., Caplinger, M. A., Bai-
 397 ley, Z. J., . . . Wolff, M. J. (2021, February). The mars 2020 perseverance rover
 398 mast camera zoom (Mastcam-Z) multispectral, stereoscopic imaging investigation.
 399 *Space Sci. Rev.*, *217*(1), 1–40.
- 400 Bistacchi, A., Mittempergher, S., & Martinelli, M. (2022, April). *Digital outcrop*
 401 *model reconstruction and interpretation*. Wiley.
- 402 Calef, F. J., Parker, T. J., Schroeder, J., Williams, N., & Golombek, M. P. (2023,
 403 March). *Spatial products and services for the mars2020 perseverance rover* (Vol.
 404 2806). ui.adsabs.harvard.edu.
- 405 Caravaca, G., Le Mouélic, S., Mangold, N., Jonas, L., Laetitia, L. D., & Marion, M.
 406 (2020, March). 3D digital outcrop model reconstruction of the kimberley outcrop
 407 (gale crater, mars) and its integration into virtual reality for simulated geological
 408 analysis. *Planet. Space Sci.*, *182*, 104808.
- 409 Caravaca, G., Le Mouélic, S., Rapin, W., Dromart, G., Gasnault, O., Fau, A., . . .
 410 Lanza, N. L. (2021, October). Long-distance 3D reconstructions using photogram-
 411 metry with curiosity’s ChemCam remote Micro-Imager in gale crater (mars).
 412 *Remote Sens. (Basel)*, *13*(20), 4068.
- 413 Caravaca, G., Mangold, N., Dehouck, E., Schieber, J., Zaugg, L., Bryk, A. B., . . .
 414 Lanza, N. L. (2022, September). From lake to river: Documenting an environmen-
 415 tal transition across the Jura/Knockfarril hill members boundary in the glen torri-
 416 don region of gale crater (mars). *J Geophys Res Planets*, *127*(9), e2021JE007093.
- 417 Crumpler, L. S., Horgan, B. H. N., Simon, J. I., Stack, K. M., Alwmark, S., Gilles,
 418 D., . . . Williams, N. R. (2023, October). In situ geologic context mapping transect
 419 on the floor of jezero crater from mars 2020 perseverance rover observations. *J.*
 420 *Geophys. Res. Planets*, *128*(10).
- 421 Farley, K. A., Stack, K. M., Shuster, D. L., Horgan, B. H. N., Hurowitz, J. A., Tar-
 422 nas, J. D., . . . Zorzano, M.-P. (2022, September). Aqueously altered igneous rocks
 423 sampled on the floor of jezero crater, mars. *Science*, *377*(6614), eabo2196.
- 424 Farley, K. A., Williford, K. H., Stack, K. M., Bhartia, R., Chen, A., de la Torre, M.,
 425 . . . Wiens, R. C. (2020, December). Mars 2020 mission overview. *Space Sci. Rev.*,
 426 *216*(8), 142.
- 427 Goudge, T. A., Mohrig, D., Cardenas, B. T., Hughes, C. M., & others. (2018).
 428 Stratigraphy and paleohydrology of delta channel deposits, jezero crater, mars.
 429 *Icarus*.
- 430 Goudge, T. A., Mustard, J. F., Head, J. W., & others. (2015). Assessing the min-
 431 eralogy of the watershed and fan deposits of the jezero crater paleolake system,
 432 mars. *Journal of*.
- 433 Hayes, A. G., Corlies, P., Tate, C., Barrington, M., Bell, J. F., Maki, J. N., . . .
 434 Winchell, K. (2021, February). Pre-flight calibration of the mars 2020 rover
 435 mastcam zoom (Mastcam-Z) multispectral, stereoscopic imager. *Space Sci. Rev.*,
 436 *217*(2), 1–95.
- 437 Hayes, A. G., Grotzinger, J. P., Edgar, L. A., Squyres, S. W., Watters, W. A., &
 438 Sohl-Dickstein, J. (2011, April). Reconstruction of eolian bed forms and paleo-
 439 currences from cross-bedded strata at victoria crater, meridiani planum, mars. *J.*
 440 *Geophys. Res.*, *116*(E00F21).
- 441 Horgan, B., Udry, A., Rice, M., Alwmark, S., Amundsen, H. E. F., Bell, J. F., III,
 442 . . . Wiens, R. C. (2023, July). Mineralogy, morphology, and emplacement history
 443 of the maaz formation on the jezero crater floor from orbital and rover observa-
 444 tions. *J. Geophys. Res. Planets*.
- 445 Kinch, K. M., Madsen, M. B., Bell, J. F., Maki, J. N., Bailey, Z. J., Hayes, A. G.,
 446 . . . Sørensen, A. N. (2020). Radiometric calibration targets for the Mastcam-Z
 447 camera on the mars 2020 rover mission. *Space Sci. Rev.*, *216*, 1–51.
- 448 Le Mouélic, S., Enguehard, P., Schmitt, H. H., Caravaca, G., Seignovert, B., Man-
 449 gold, N., . . . Civet, F. (2020, June). Investigating lunar boulders at the apollo 17

- 450 landing site using photogrammetry and virtual reality. *Remote Sensing*, 12(11),
451 1900.
- 452 Maki, J. N., Gruel, D., McKinney, C., Ravine, M. A., Morales, M., Lee, D., ...
453 Algermissen, S. (2020, November). The mars 2020 engineering cameras and mi-
454 crophone on the perseverance rover: A Next-Generation imaging system for mars
455 exploration. *Space Sci. Rev.*, 216(8), 137.
- 456 Mangold, N., Gupta, S., Gasnault, O., Dromart, G., Tarnas, J. D., Sholes, S. F.,
457 ... Williford, K. H. (2021, November). Perseverance rover reveals an ancient
458 delta-lake system and flood deposits at jezero crater, mars. *Science*, 374(6568),
459 711–717.
- 460 Maurice, S., Wiens, R. C., Bernardi, P., Caïs, P., Robinson, S., Nelson, T., ...
461 Wong, K. W. (2021, April). The SuperCam instrument suite on the mars 2020
462 rover: science objectives and mast-unit description. *Space Sci. Rev.*, 217(3), 47.
- 463 Over, J.-S. R., Ritchie, A. C., Kranenburg, C. J., Brown, J. A., Buscombe, D. D.,
464 Noble, T., ... Wernette, P. A. (2021). *Processing coastal imagery with agisoft*
465 *metashape professional edition, version 1.6—structure from motion workflow docu-*
466 *mentation* (No. 2021-1039). US Geological Survey.
- 467 Paar, G., Mett, M., Ortner, T., Kup, D., & Kontrus, H. (2022, June). High-
468 resolution real-time multipurpose tunnel surface 3D rendering. *Geomech. Tunn.*,
469 15(3), 290–297.
- 470 Paar, G., Ortner, T., Tate, C., Deen, R. G., Abercrombie, P., Vona, M., ... Barnes,
471 R. (2023). Three-Dimensional data preparation and immersive Mission-Spanning
472 visualization and analysis of mars 2020 Mastcam-Z stereo image sequences. *Life*
473 *Support Biosph. Sci.*, 10(3), e2022EA002532.
- 474 Prepared by the Mars Sample Return Campaign Science Group (MCSG), Czaja,
475 A. D., Zorzano, M.-P., Kminek, G., Meyer, M. A., Beaty, D. W., ... Members
476 (2023, June). Report of the science community workshop on the proposed first
477 sample depot for the mars sample return campaign. *Meteorit. Planet. Sci.*, 58(6),
478 885–896.
- 479 Quantin-Nataf, C., Alwmark, S., Calef, F. J., & others. (2023). The complex ex-
480 humation history of jezero crater floor unit and its implication for mars sample
481 return. *Journal of*.
- 482 Quinn, D. P., & Ehlmann, B. L. (2019, August). A PCA-based framework for deter-
483 mining remotely sensed geological surface orientations and their statistical quality.
484 *Earth Space Sci.*, 6(8), 1378–1408.
- 485 Ruoff, N. A., Deen, R. G., Pariser, O. (2023). Mars 2020 camera software inter-
486 face specification (SIS) [Computer software manual]. JPL Doc ID: D-99960, Jet
487 Propulsion Laboratory.
- 488 Schon, S. C., Head, J. W., & Fassett, C. I. (2012, July). An overfilled lacustrine
489 system and progradational delta in jezero crater, mars: Implications for noachian
490 climate. *Planet. Space Sci.*, 67(1), 28–45.
- 491 Stack, K. M., Williams, N. R., Calef, F., 3rd, Sun, V. Z., Williford, K. H., Farley,
492 K. A., ... Yingst, R. A. (2020, December). Photogeologic map of the persever-
493 ance rover field site in jezero crater constructed by the mars 2020 science team.
494 *Space Sci. Rev.*, 216(8).
- 495 Traxler, C., Ortner, T., Hesina, G., Barnes, R., Gupta, S., Paar, G., ... Willner, K.
496 (2022, April). *The PProViDE framework: Accurate 3D geological models for virtual*
497 *exploration of the martian surface from rover and orbital imagery*. Wiley.
- 498 Wiens, R. C., Maurice, S., Robinson, S. H., Nelson, A. E., Cais, P., Bernardi, P., ...
499 Willis, P. (2021). The SuperCam instrument suite on the NASA mars 2020 rover:
500 Body unit and combined system tests. *Space Sci. Rev.*, 217(1), 4.